Hydrogen diffusion in potassium intercalated graphite studied by quasielastic neutron scattering

Justin Purewal, J. Brandon Keith, Channing C. Ahn, Craig M. Brown, Madhusudan Tyagi et al.

Citation: J. Chem. Phys. **137**, 224704 (2012); doi: 10.1063/1.4767055
View online: http://dx.doi.org/10.1063/1.4767055
View Table of Contents: http://jcp.aip.org/resource/1/JCPSA6/v137/i22
Published by the American Institute of Physics.

Hydrogen diffusion in potassium intercalated graphite studied by quasielastic neutron scattering

Justin Purewal,[1,a)] J. Brandon Keith,[1] Channing C. Ahn,[1] Craig M. Brown,[2] Madhusudan Tyagi,[2,b)] and Brent Fultz[1]
[1]*California Institute of Technology, W. M. Keck Laboratory 138-78, Pasadena, California 91125, USA*
[2]*NIST Center for Neutron Research, 100 Bureau Drive, Gaithersburg, Maryland 20899, USA*

(Received 22 September 2012; accepted 29 October 2012; published online 14 December 2012)

The graphite intercalation compound KC_{24} adsorbs hydrogen gas at low temperatures up to a maximum stoichiometry of $KC_{24}(H_2)_2$, with a differential enthalpy of adsorption of approximately -9 kJ mol^{-1}. The hydrogen molecules and potassium atoms form a two-dimensional condensed phase between the graphite layers. Steric barriers and strong adsorption potentials are expected to strongly hinder hydrogen diffusion within the host KC_{24} structure. In this study, self-diffusion in a $KC_{24}(H_2)_{0.5}$ sample is measured experimentally by quasielastic neutron scattering and compared to values from molecular dynamics simulations. Self-diffusion coefficients are determined by fits of the experimental spectra to a honeycomb net diffusion model and found to agree well with the simulated values. The experimental H_2 diffusion coefficients in KC_{24} vary from 3.6×10^{-9} m^2 s^{-1} at 80 K to 8.5×10^{-9} m^2 s^{-1} at 110 K. The measured diffusivities are roughly an order of magnitude lower that those observed on carbon adsorbents, but compare well with the rate of hydrogen self-diffusion in molecular sieve zeolites. © *2012 American Institute of Physics*. [http://dx.doi.org/10.1063/1.4767055]

I. INTRODUCTION

Microporous carbons are candidates for adsorption-based hydrogen storage applications. However, the adsorption enthalpies (ΔH) are well below the -15 to -20 kJ mol^{-1} range required for adsorption-based hydrogen storage near room temperature.[1,2] There have been a number of proposed methods to increase the adsorption enthalpy.[3] These include: (1) incorporating an expanded or pillared graphite structure with optimized interlayer separation;[4–7] (2) introducing a chemically modified structure that interacts with H_2 molecules via strong electrostatic forces.[8] The KC_{24} graphite intercalation compound contains both of these features, making it an interesting system for studying hydrogen adsorption in chemically modified, nano-structured carbons. Graphite intercalation compounds (GIC) are layered crystalline materials formed by the insertion of atomic or molecular guests between the layers of the host graphite. Stage 1 potassium intercalated graphite (KC_8) does not adsorb H_2 at low temperatures, since the dense potassium monolayer occupies all the available space within the graphite gallery. In contrast, the stage 2 GIC (nominal stoichiometry KC_{24}) contains a potassium intercalate layer between every second pair of host graphite layers. As KC_{24} contains one-third fewer potassium atoms per gallery compared to KC_8, the potassium monolayer contains cavities which can occlude small molecules. As shown in Fig. 1(a), the center-to-center spacing for a potassium intercalated layer in KC_{24} is 5.4 Å, compared to 3.35 Å for a non-intercalated layer. The expanded interlayer spacing creates a slit-pore-like structure, which permits H_2 adsorption at 77 K up to a composition of $KC_{24}(H_2)_2$, equivalent to roughly 1 wt. % excess hydrogen uptake.[9–11] Gas adsorption by KC_{24} is known to exhibit molecular-sieving behavior due to size mismatch between the diameters of the sorptive gas molecules and the gap between graphite layers.[9] Extensive inelastic neutron scattering measurements on H_2/MC_{24} (M = K, Rb, Cs) all indicate strong barriers to out-of-plane H_2 rotation, as evidenced by the large splitting of the $J = 0$ to $J = 1$ rotational transition.[12]

Two kinds of structures for the in-plane alkali metal lattice have been reported: (1) a $\sqrt{7} \times \sqrt{7}$ $R19.11^\circ$ structure (see Fig. 1(b)) with discommensurations; (2) an incommensurate alkali structure including modulation effects. In both superstructures, the alkali metal atoms form a triangular lattice in the short-range with metal-metal distance of roughly 6 Å. There are two triangular interstitial sorption sites per metal atom, consistent with the observed adsorption capacity. The resulting geometric pattern of small cavities connected by narrow windows (similar to those in zeolites and metal-organic frameworks) allows for long-range diffusion of H_2 molecules within the graphite layers. The environment surrounding the H_2 sorption sites in KC_{24} is impacted by a strongly polarized electric field between graphite layers, generated by charge transfer from potassium to graphite.[13,14] Overlapping graphite corrugation potentials from the host GIC structure are another significant feature. Hydrogen adsorption in KC_{24} has an isosteric heat[9,10,15] of approximately -9 kJ mol^{-1}, in comparison to -4 kJ mol^{-1} for adsorption on graphite.[16] Although the hydrogen molecule is nonpolar, the importance of hydrogen sorption sites with strong

a)Present address: HRL Laboratories LLC, Malibu, California 90265, USA. Electronic mail: jjpurewal@hrl.com.
b)Also at Department of Materials Science, University of Maryland, College Park, Maryland 20742, USA.

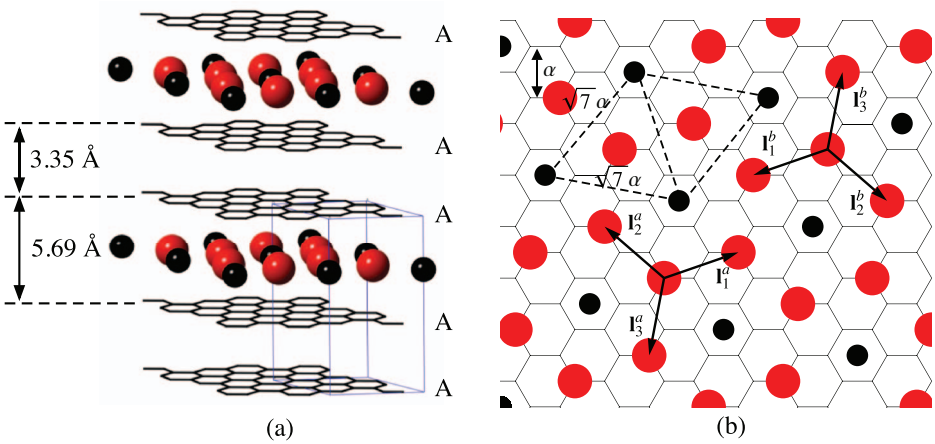

FIG. 1. (a) KC_{24} structure with the AlA stacking sequence used for the simulation supercell. The interlayer spacing for the potassium layer expands from 5.40 Å to 5.69 Å following adsorption of H_2. (b) The in-plane $\sqrt{7} \times \sqrt{7}$ $R19.11^\circ$ structure used for simulations and for the honeycomb net jump diffusion model. Hydrogen molecule sites are represented by red circles and potassiums by black circles. The hydrogen sites form a two-dimensional honeycomb net structure. The sets of jump vectors for the two basis points are labeled $\mathbf{l}_i^a$ and $\mathbf{l}_i^b$, respectively.

Coulomb interactions has been reported for metal-organic-frameworks[17] and ion-exchanged zeolites.[18] Hydrogen uptake by KC_{24} at low temperatures (~77 K) has been well established as a physisorption process that occurs without H_2 dissociation.[10] At 300 K, however, hydrogen chemisorption occurs in KC_{24}, producing an equilibrium stoichiometry of $KC_{24}H_{0.51}$.[19] The nature of H_2 storage in KC_{24} might be described almost as an intermediate between physisorption and chemisorption.

Hydrogen diffusion in KC_{24} is expected to be characterized by a higher activation barrier and a smaller self-diffusion coefficient than in most other carbon adsorbents. First, the narrow windows between H_2 sorption sites (steric barriers) should present a large energy barrier for hydrogen molecules as they hop between neighboring adsorption sites. Second, H_2 adsorption sites within the potassium superlattice should have a deep potential well, as indicated by equilibrium pressure-composition-temperature (PCT) data. To date, however, there have been few experimental measurements of H_2 diffusion in the stage-2 AM-GICs. Quasielastic neutron scattering (QENS) is an experimental technique that is particularly well suited to quantitatively studying the motions of hydrogen adsorbed in host frameworks. Using QENS, Beaufils *et al.* estimated a self-diffusion constant for H_2 in CsC_{24} equal to $D = 1 \times 10^{-9}$ $m^2\,s^{-1}$ at 125 K.[12] Previously, we measured the QENS spectra of $KC_{24}(H_2)_1$, in which H_2 diffusion was detected on two characteristic residence times (~10 ps, ~1000 ps) within the same temperature range.[15] However, the hydrogen concentration in that experiment was too large to make an accurate estimate of the self-diffusion constant.

In this work, hydrogen diffusion in KC_{24} is investigated using quasielastic neutron scattering and molecular dynamics simulations. Experimental QENS spectra are fitted to a two-dimensional, honeycomb (HC) net jump diffusion model to investigate the characteristic frequencies and jump lengths of H_2 diffusion in KC_{24}. Molecular dynamics simulations of the KC_{24}/H_2 system are used to estimate the steady state hydrogen self-diffusion. Additional data on the temperature variation of hydrogen diffusion in KC_{24} is provided by measurements of neutron elastic scattering versus temperature. Hydrogen uptake kinetics are also investigated by volumetric adsorption measurements. The current study provides an opportunity to directly compare experimental and simulated values of hydrogen diffusion at the molecular level, along with comparisons to macroscopic adsorption kinetics measurements.

II. METHODS

A. Experimental

Samples of KC_{24} were synthesized using a modified single-temperature-zone technique. The starting materials were thermally purified natural flake graphite (Superior Graphite Co., 99.95% –99.99% purity, 50 mesh) and potassium metal (Alfa Aeser, 99.9%). Stoichiometric amounts of graphite and potassium (22:1 molar ratio) were weighed out in an argon glovebox, transferred to a glass ampoule, evacuated to 0.1 mbar, and sealed. Samples were heated at 623 K for 24 h and shaken occasionally to ensure homogeneity. Phase purity of the stage-2 intercalation compound was confirmed by powder X-ray diffraction (see Fig. S9 of the supplementary material). The dominant features in the diffraction pattern are the (00*l*) basal-plane reflections which indicate an interlayer spacing of 5.41 Å for the potassium-containing layer. Peaks from the stage-1 or stage-3 and higher compounds are not visible in the diffraction pattern. Pressure-composition-temperature diagrams for H_2/KC_{24} were measured at 77 K and 87 K by the standard volumetric method, using a 0.787 g powder KC_{24} sample.

Quasielastic neutron scattering measurements were performed on the disc chopper spectrometer (DCS) at the NIST Center for Neutron Research.[20] A powder KC_{24} sample with a mass of 2.2506 g was transferred in a high-purity helium glovebox to an annular-geometry sample cell sealed with an indium o-ring. The sample thickness was chosen for ~10% total scattering. The sample can was mounted onto a sample

stick which was adapted for a top-loading, closed-cycle helium refrigerator system. The sample can was connected with a stainless steel capillary line to a gas handling rig containing a calibrated volume and a high resolution pressure transducer. Hydrogen loading was performed at 60 K by filling the calibrated volume with the precise amount of H_2 gas needed for a $KC_{24}(H_2)_{0.5}$ composition, opening the valve to the sample, and monitoring the pressure as it dropped to approximately 0 mbar. The DCS measurements were collected using an incident neutron wavelength of $\lambda = 6.0$ Å with an energy resolution of approximately 65 μeV at the elastic line. This provided a neutron energy loss range of 1.35 meV, and a momentum transfer (Q) range of 0.1–2.0 Å^{-1}. The DAVE software package was used for data reduction and peak fitting.[21] In addition, elastic scattering intensity was measured on the High Flux Backscattering Instrument (HFBS) in the fixed-window mode.[22] For these measurements, the Doppler drive was stopped and elastic scattering was recorded and summed over all detector banks. The energy resolution at the elastic peak is roughly 0.85 μeV for HFBS.

Scattering from KC_{24} was measured at 40 K and 60 K on DCS. The neutron scattering spectra at the different temperatures were identical within the instrument resolution. Scattering from $KC_{24}(H_2)_{0.5}$ was collected at 80 K, 90 K, 100 K, and 110 K. By monitoring the pressure, we confirmed that there was not any significant desorption of H_2 at these temperatures. Since the incoherent scattering cross-section of hydrogen is very large, a substantial fraction of the total scattering is from hydrogen. The background signal from empty KC_{24} is subtracted to estimate the scattering from hydrogen. As the metal-containing graphite galleries expand approximately 5% upon H_2 adsorption, the KC_{24} diffraction peaks shift to slightly lower Q values, causing an excess background signal on the high-Q side. Therefore, it was necessary to mask the detector banks containing the diffraction peaks for both the KC_{24} and $KC_{24}(H_2)_{0.5}$ samples. The reduced $S(Q, E)$ was binned into Q increments of 0.15 Å^{-1} and into energy increments of 0.01 meV. Here $S(Q, E)$ denotes the incoherent scattering function, while $\hbar Q$ represents the momentum transferred from the neutron to the scatterer, and E represents the neutron energy loss.

B. Molecular dynamics simulations

Parameters for the H_2–H_2 and H_2–KC_{24} interactions were taken from the literature without further optimization (see Table I). The C–C, K–K, and C–K solid-solid interactions were described using 12-6 Lennard-Jones (LJ) potentials from Ref. 23, which were based on fits to experimental data for graphite and potassium-intercalated graphite. The C–H_2 solid-fluid interaction was modeled with an exp-6 LJ potential from Ref. 24, based on MP2/aug-cc-p calculations of the H_2-graphite interaction. The H_2–H_2 interactions were described with a 12-6 LJ potential from Ref. 25 which was optimized using bulk hydrogen data. Due to the importance of quantum effects in the $KC_{24}(H_2)_x$ system, as evidenced by the strong isotope effect for H_2/D_2 adsorption, the Feynman-Hibbs effective potential is utilized for the H_2–H_2 interaction, using the numerical approximation from Ref. 25. Electrostatic interactions are not explicitly included here; simulations for H_2/MOF systems have suggested that electrostatic terms are not necessarily required to reproduce experimental data.[26] The cutoff for the 12-6 and exp-6 LJ potentials was set at 12 Å. The graphite structure was held fixed during the simulations.

TABLE I. Pair-potential parameters for $KC_{28}(H_2)_x$ for the molecular dynamics simulations.

12-6 LJ potential[a]			
Atom 1	Atom 2	ϵ (meV)	r_m (Å)
C	C	3.00	3.805
K	K	3.04	4.001
K	C	3.02	3.902
H2	H2	3.33	3.123
K	H2	6.20	3.440

exp-6 potential[b]				
Atom 1	Atom 2	A (eV)	λ (Å^{-1})	B (eV · Å^6)
C	H2	1059.13	3.547	17.417

[a]Notation for 12-6 LJ potential: $V_{LJ} = \epsilon[(r_m/r)^{12} - 2(r_m/r)^6]$.
[b]Notation for exp-6 potential: $V_{exp\text{-}6} = A\exp(-\lambda r) - Br^{-6}$.

The initial in-plane potassium configurations were set according to the $\sqrt{7} \times \sqrt{7}$ $R19.11^\circ$ structure shown in Fig. 1; as described in Sec. III, this structure has an associated stoichiometry of KC_{28}. For the out-of-plane structure, the A–A stacking sequence was used with an interlayer spacing of 5.69 Å for the intercalated layer and 3.35 Å for the non-intercalated layer (consistent with powder XRD data).[27] The simulation supercell was sized $a = 52.0$ Å, $b = 45.0$ Å, $c = 9.04$ Å, with periodic boundary conditions. This supercell contains 64 potassium atoms, and 1792 carbon atoms. Hydrogen molecules were placed randomly at the centers of the triangular interstitial sites at various H_2/K ratios. Molecular dynamics simulations were performed using the General Utility Lattice Program.[28] Simulations were run using an *NVT* ensemble with a leapfrog-verlet integrator and a time-step of 1 fs. Temperature was controlled with a Nose-Hoover thermostat. The simulations were equilibrated for 50 ps (50 000 steps) followed by a production run of 500 ps (500 000 steps).

III. JUMP DIFFUSION MODEL

The diffusion of H_2 molecules in KC_{24} is approximately two-dimensional, as it is unlikely for a hydrogen molecule to pass through two graphite planes into a neighboring intercalate layer. To develop a model for the in-plane H_2 diffusion, the $\sqrt{7} \times \sqrt{7}$ $R19.11^\circ$ structure is used to describe the local in-plane arrangements of potassium atoms in KC_{24}. We note that the $\sqrt{7} \times \sqrt{7}$ structure actually has a KC_{28} stoichiometry, but regions of higher metal density in the domain wall regions are assumed to balance this to produce the nominal KC_{24} stoichiometry. Recent work has pointed to the existence of a single H_2 adsorption site located at the center of the triangular interstitial site in the potassium lattice.[14] As illustrated in Fig. 1, the H_2 adsorption sites form a honeycomb net. There are two nonequivalent sets of jump vectors connecting a site on the honeycomb net to its three nearest neighbor (NN) sites

in the plane, with $\{\mathbf{l}_i^a\} = \{-\mathbf{l}_i^b\}$,

$$\begin{aligned} \mathbf{l}_1^a &= (l, 0, 0), & \mathbf{l}_1^b &= (-l, 0, 0), \\ \mathbf{l}_2^a &= (-l/2, -\sqrt{3}l/2, 0), & \mathbf{l}_2^b &= (l/2, \sqrt{3}l/2, 0), \\ \mathbf{l}_3^a &= (-l/2, \sqrt{3}l/2, 0), & \mathbf{l}_3^b &= (l/2, -\sqrt{3}l/2, 0), \end{aligned} \quad (1)$$

where the in-plane graphite lattice constant is $\alpha = 2.462$ Å, and the distance between NN sorption sites is $l = \alpha\sqrt{7/3} = 3.7$ Å.

The original Chudley-Elliot jump diffusion model assumes a Bravais lattice,[29,30] but has been extended to the case of a non-Bravais lattices,[31] and to the honeycomb net in particular.[32,33] The models are only valid in the dilute limit where site-blocking and correlation between consecutive jumps are absent. These conditions are approximately satisfied by the $KC_{24}(H_2)_{0.5}$ composition, where the hydrogen concentration is sufficiently dilute, but they do not necessarily hold for hydrogen compositions greater than $KC_{24}(H_2)_1$. It should be noted that the jump diffusion model only considers proton hopping on a lattice, and does not take into account the rotational motions of H_2 molecules. If rotational diffusion were to contribute to the quasielastic broadening, then the actual translational diffusivity would be slightly lower than the estimated value. Elastic scattering by H_2 at 80–110 K should correspond to $J = 1 \rightarrow J = 1$, which is proportional to the incoherent cross-section. The $J = 0 \rightarrow J = 0$ scattering is proportional to the small coherent cross-section[34] and should be only a small part of the QENS scattering.

Following the analysis by Stuhr[32] and Cappelletti,[33] the momentum transfer (Q) and energy transfer (E) dependent incoherent scattering function for jump diffusion on a HC net is equal to a sum of two Lorentzian functions

$$S_{\text{inc}}(\mathbf{Q}, E) = \frac{1}{\pi}\sum_{j=1}^{2}\frac{w_j\Gamma_j}{E^2 + \Gamma_j^2}, \quad (2)$$

where the weights w_j and linewidths Γ_j of the two Lorentzians are given by

$$\begin{aligned} w_1 &= \tfrac{1}{2}(1 + \text{Re}(\mathbf{K})/|\mathbf{K}|), & \Gamma_1 &= L - |\mathbf{K}|, \\ w_2 &= \tfrac{1}{2}(1 - \text{Re}(\mathbf{K})/|\mathbf{K}|), & \Gamma_2 &= L + |\mathbf{K}|. \end{aligned}$$

The values for L and $\mathbf{K}$ are calculated as

$$L = \frac{\hbar}{\tau}, \quad \mathbf{K} = \frac{\hbar}{3\tau}\sum_{i=1}^{3}\exp(-i\mathbf{Q}\cdot\mathbf{l}_i), \quad (3)$$

where the sum is taken over $\{l_i\} = \{l_i^a\}$. Average residence time is equal to τ. The self-diffusion coefficient in two dimensions is then equal to $D = l^2/(4\tau)$. We write the scattering vector $\mathbf{Q}$ for an arbitrary orientation as

$$\mathbf{Q} = (Q\cos\phi\sin\theta,\, Q\sin\phi\sin\theta,\, Q\cos\theta).$$

The magnitude and real part of $\mathbf{K}$ are then given by

$$|\mathbf{K}| = \frac{1}{3\tau}\left[1 + 4\cos^2 b + 4\cos b\cos\tfrac{3a}{2}\right]^{1/2}, \quad (4)$$

$$\frac{\text{Re}(\mathbf{K})}{|\mathbf{K}|} = \frac{\cos a + 2\cos\frac{a}{2}\cos b}{\left[1 + 4\cos^2 b + 4\cos b\cos\frac{3a}{2}\right]^{1/2}}, \quad (5)$$

where $a = Ql\cos\phi\sin\theta$ and $b = 3/2Ql\sin\phi\sin\theta$. The KC_{24} samples measured in this experiment are polycrystalline, so it is necessary to calculate the orientational average over θ and ϕ,

$$\langle S_{\text{inc}}(Q, E)\rangle = \frac{1}{4\pi}\int_0^{2\pi}\int_0^{\pi} S_{\text{inc}}(\mathbf{Q}, E)\sin\theta\,\mathrm{d}\theta\,\mathrm{d}\phi. \quad (6)$$

This powder average was evaluated numerically using $\Delta\theta = \pi/30$ and $\Delta\phi = 2\pi/30$. To obtain adequate fits to the experimental QENS data, we found that it was necessary to include an elastic-like term, $f\delta(E)$. The relative intensity (f) of the elastic-like component varies between 0 and 1, consistent with an elastic incoherent structure factor (EISF). Numerical convolution with the instrument resolution function, $R(Q, E)$, yields the model peak shape

$$A[(f)\delta(E) + (1 - f)\langle S_{inc}\rangle] \otimes R, \quad (7)$$

where (Q, E) are independent variables, and (τ, l, f, A) are the adjustable parameters.

In the limit of small Q, Eq. (2) should reduce to the scattering function for continuous diffusion in two dimensions

$$S_{\text{inc}}(Q, E) = \frac{1}{\pi}\frac{\hbar D(Q\sin\theta)^2}{E^2 + [\hbar D(Q\sin\theta)^2]^2}, \quad (8)$$

where θ is the angle between $\mathbf{Q}$ and the normal to the plane of diffusion, and D is the diffusion coefficient in two-dimensions. When $\mathbf{Q}$ is perpendicular to the diffusion ($\theta = 0$) elastic scattering is obtained. Lorentzians of increasing width are obtained as θ increases. The orientational average of the two-dimensional scattering law can be calculated analytically[35,36] and the resulting function has a cusp-like shape with a logarithmic singularity at $E = 0$. At finite instrument resolution, scattering from a two-dimensional system cannot be easily distinguished from actual elastic scattering arising from a non-diffusing population of hydrogen molecules.

IV. RESULTS

A. Hydrogen adsorption isotherms

Hydrogen adsorption isotherms and kinetics plots for KC_{24} are presented in Fig. 2. The adsorption isotherms at 77 K and 87 K in panel (a) are consistent with previously published results,[9,11] exhibiting a distinctive convex curvature at low concentration.[37] This is associated with the work expended in increasing the c-axis interlayer spacing during H_2 adsorption. Using the Clausius-Clapeyron equation, the isosteric heat is estimated to be between −8 and −9 kJ/mol, consistent with previous results (see Fig. S12 of the supplementary material). An interesting feature of H_2 sorption by stage-II GICs, which does not appear to have been previously reported in the literature, is the significant slowing of adsorption kinetics which occurs at higher concentrations ($x > 1$). This effect is illustrated in Fig. 2(b), which displays the H_2 fractional adsorption during three adsorption steps for RbC_{24}. Qualitatively the adsorption kinetics for all three (K,Rb,Cs) stage-2 GICs were very similar. For the initial H_2 uptake ($x < 1$), the equilibrium pressure is reached within 3 min

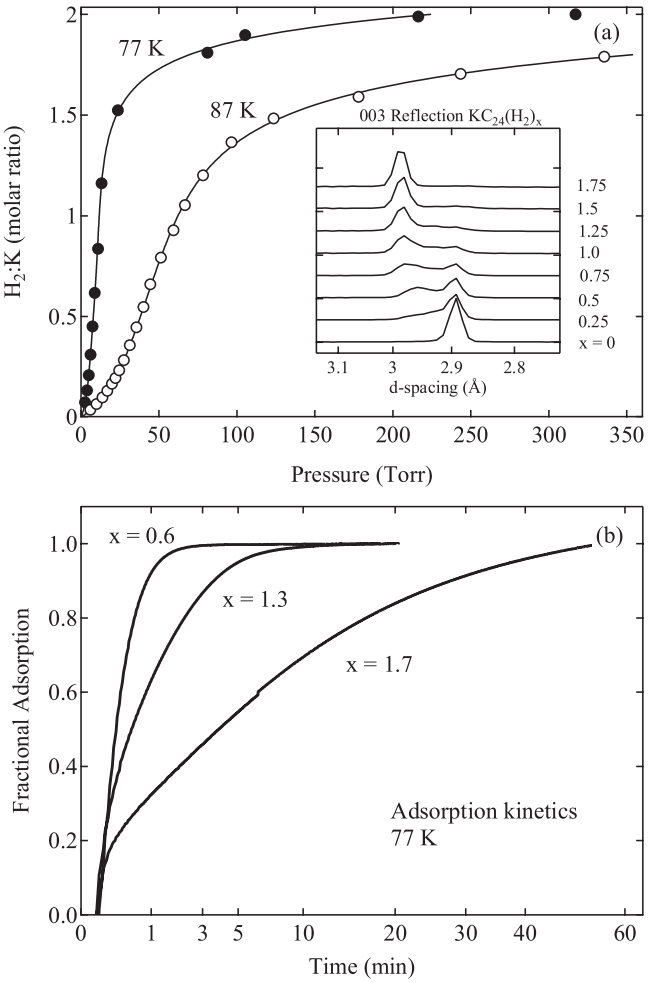

FIG. 2. (a) Hydrogen adsorption isotherms for KC_{24} at 77 K and 87 K. The adsorption amounts are plotted as a molar ratio of H_2 to potassium. (Inset) Neutron diffraction pattern of $KC_{24}(H_2)_x$ at 4 K near the (003) reflection vertically offset for a series of H_2 loadings. (b) Hydrogen adsorption kinetics for $RbC_{24}(H_2)_x$ at 77 K for three different H_2 concentrations plotted versus time (on a $\sqrt{t}$ scale).

(within the range of typical equilibration times for microporous materials). As the hydrogen concentration increases, the adsorption kinetics slow down. For the $x \approx 1.3$ loading, it requires approximately 12 min to reach equilibrium, while at $x \approx 1.7$ the adsorption is unusually slow, with an equilibrium time exceeding 60 min.

Hydrogen adsorption kinetics in KC_{24} depends on the degree of graphitization and the nature of defects in the graphite host material. However, hydrogen adsorption kinetics in high quality HOPG-based samples are known to be slow compared to powder-based samples, suggesting that crystal size strongly influences the kinetics. The AM-GIC samples used in these measurements were prepared from relatively large (50 mesh) high-purity natural flake graphite.[38] This suggests that large crystallites in the flake graphite samples may be an important factor in the slow adsorption kinetics, since H_2 must enter the KC_{24} galleries primarily though the edge sites of the layered crystal structure. Studies reporting faster H_2 uptake, on the other hand, used finely powdered KC_{24} where crystallite sizes are expected to be smaller and concentration of edge sites should be much larger.[9] The slow adsorption kinetics observed for the large KC_{24} flakes also indicate that the long bulk diffusion lengths are a significant factor. This suggests that H_2 intra-crystalline diffusion is hindered at higher concentrations ($x > 1$) where site-blocking would be significant.

B. Diffraction

Diffraction patterns for $KC_{24}(H_2)_x$ at 4 K were obtained by plotting the integrated elastic intensity measured on DCS versus momentum transfer. Hydrogen was loaded in KC_{24} at 60 K and allowed to equilibrate before lowering the temperature to 4 K at a rate of approximately 3 K/min. The (003) reflection is plotted in the inset of Fig. 2(a) for a series of H_2 loadings. Scattering from H_2 appears to contribute only to the diffuse background. For empty KC_{24}, the (003) reflection has a *d*-spacing of 2.90 Å, respectively. This indicates an average KC_{24} interlayer spacing of 5.34 Å, roughly consistent with the values obtained by XRD. As H_2 is introduced to the sample, there is a gradual transfer of intensity to a second peak at 2.99 Å. The fully hydrogenated sample has an interlayer spacing of about 5.63 Å. Therefore, the KC_{24} layers expand by about 5% with H_2 adsorption, in good agreement with results from Refs. 9 and 14. This result confirms that H_2 is being adsorbed between the layers of KC_{24} and expanding the interlayer spacing. The transfer of intensity between two distinct sets of peaks indicates that $KC_{24}(H_2)_x$ contains coexistent regions of the hydrogenated and pure KC_{24} phase. This last point suggests that the local H_2 concentration may be higher than suggested by the nominal $KC_{24}(H_2)_x$ stoichiometry, since the H_2 may not be uniformly distributed. This could have consequences for accurately determining the H_2 diffusivity from QENS data.

C. Elastic intensity

Using the fixed window mode of operation on the HFBS instrument, we measured the elastic scattering of $KC_{24}(H_2)_{0.5}$ system versus temperature (Fig. 3). The curve for empty KC_{24} has no significant features between 4 and 80 K. In contrast, the $KC_{24}(H_2)_{0.5}$ curve shows a decrease in the elastic intensity starting at ~35 K. The drop in elastic signal is accompanied by the emergence of quasielastic intensity, indicating the presence of hydrogen diffusion.[15] The negligible change in the equilibrium H_2 vapor pressure during the runs confirmed that H_2 desorption at higher temperatures did not contribute to the decrease in elastic scattering at higher temperatures.

Hydrogen adsorption on aromatic alkali-metal charge transfer complexes is known to facilitate the ortho-para conversion at low temperatures.[39] At the same time, the equilibrium concentration of *o*-H_2 may be enhanced over *p*-H_2 due to the strongly hindered molecular rotation of hydrogen within KC_{24}.[40] To explore the impact of ortho-para conversion on the elastic intensity profiles, we measured the scattering intensity at various heating and cooling rates. Normal H_2 was loaded at 80 K, and the elastic intensity did not show any immediate decrease. Therefore, the *o*/*p* ratio remained at 3:1 for the adsorbed hydrogen at 80 K. The sample

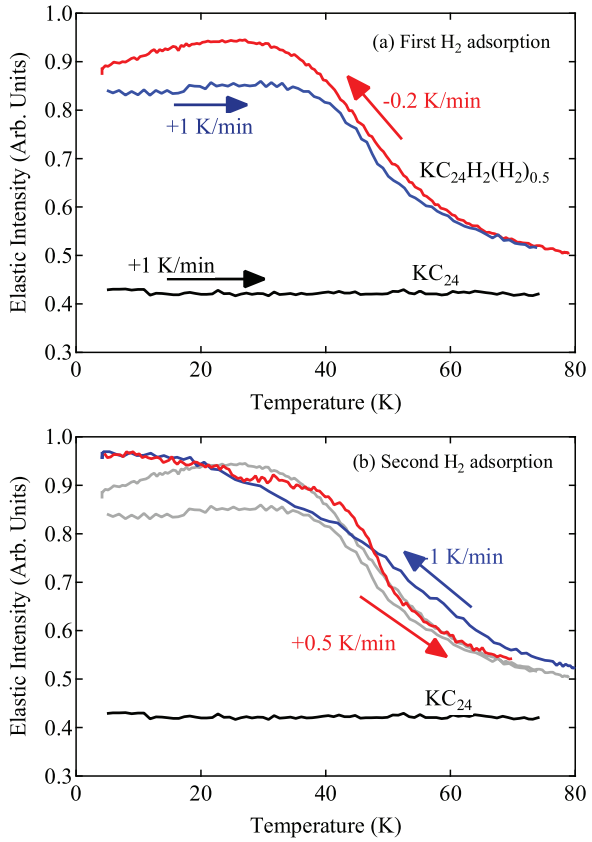

FIG. 3. Elastic neutron scattering intensities for $KC_{24}(H_2)_{0.5}$ versus sample temperature. (a) First hydrogen loading: Sample cooled slowly at 0.2 K/min down to 4 K. The sample was left for several hours before heating at 1 K/min. (b) Second hydrogen loading: Sample cooled at 1 K/min down to 4 K; then heated at 0.5 K/min. Elastic intensity curves from the first loading are shown as the gray traces.

was slowly cooled at −0.2 K/min from 80 K to 4 K over a span of approximately 8 h. As shown in Fig. 3(a), the elastic intensity initially increases as the translation diffusion and center-of-mass vibration of the H_2 molecules is reduced. Conversion to p-H_2 then becomes visible at 30 K as the elastic intensity starts to decrease. Once the sample reached 4 K, it was left for several hours. During this interval the elastic intensity continued to decrease slowly. The $KC_{24}(H_2)_{0.5}$ sample was then heated rapidly at 1 K/min back to 80 K. The small increase in elastic intensity near 20 K which may be attributable to conversion of p-H_2 back to o-H_2. Based on the primary rotational tunneling transition for $KC_{24}(H_2)_{0.5}$ located at $E_{o\text{-}p} \approx 1.5$ meV,[14] the equilibrium o/p ratio may be estimated as $o/p = 3\exp(-E_{o\text{-}p}/kT)$. At $T = 80$ K the ratio is close to 2.5, decreasing to $o/p \approx 1.7$ at 30 K and $o/p \approx 0$ at 4 K. Full conversion of o-H_2 to p-H_2 would be expected to largely quench the elastic scattering intensity from H_2. However, the presence of significant residual elastic intensity at 4 K indicates that a large fraction of o-H_2 remains unconverted. It is unclear whether this is due to the slow conversion rate, or from an enhanced equilibrium concentration of o-H_2 arising from the hindered molecular rotations in KC_{24}.

Following the first measurement cycle, the adsorbed H_2 was released by heating to 150 K under continuous vacuum. Empty KC_{24} was then re-loaded with normal H_2 at 80 K, and this time it was cooled rapidly at a rate of −1 K/min, as shown in Fig. 3(b). The sample cooling appeared to outpace the isomer conversion, as there was no visible decrease in the elastic intensity below 30 K. The increase in elastic intensity was more gradual for the −1 K/min curve compared to the curve for the initial −0.2 K/min measurement. Once the 4 K setpoint was reached, the sample was heated at a rate +0.5 K/min. This +0.5 K/min curve is qualitatively similar to the +1 K/min curve from the first loading. Both curves can be divided into three regions: (region 1) A relatively flat area between 4 K and 40 K where diffusion is below the measurable time window of the instrument; (region 2) a steep region between 40 K and 55 K; (region 3) a flat area between 55 K and 80 K. The differences between the curves in Fig. 3 are complex, and it is difficult at present to conclude whether they arise from o/p composition, or from the temperature dependence of the translational diffusion. One point of agreement between all of the measurements is that, within the instrument resolution, H_2 translational diffusion seems to start between 35 K and 40 K. In Sec. IV D, we present QENS measurements performed at a higher temperature range (80 K–110 K) where the diffusivity is fast enough to be detected at an energy loss range on the order of 0.1 meV.

D. QENS measurements

Individual QENS spectra of $KC_{24}(H_2)_{0.5}$ for $Q = 1.61$ Å^{-1} and measured between 80–110 K on DCS are displayed in Fig. 4. Instrumental resolution is drawn as a solid red line. The data consist entirely of scattering from hydrogen, since the signal from bare KC_{24} was subtracted as background. At each temperature, the spectrum contains a broad quasielastic component and a sharp elastic-like component. The intensity from the elastic-like component decreases with temperature and is fairly small at 110 K. The amount of adsorbed hydrogen was confirmed by volumetric measurements to be nearly constant at $KC_{24}(H_2)_{0.5}$ in all of the spectra. Conversion from o-H_2 to p-H_2 did not appear significant at these temperatures, as the majority of scattering from hydrogen was incoherent scattering from o-H_2.

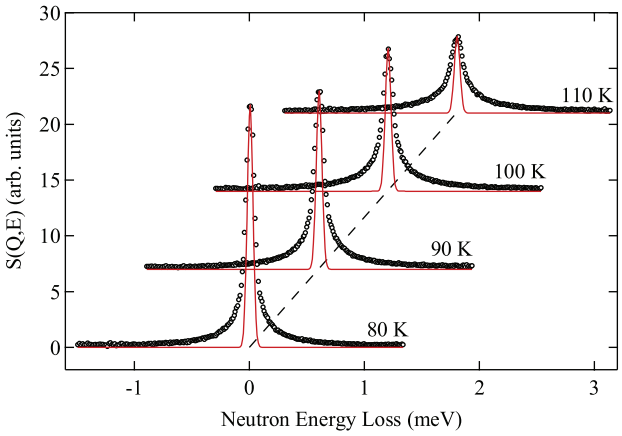

FIG. 4. QENS spectra of $KC_{24}(H_2)_{0.5}$ at $Q = 1.61$ Å^{-1} measured on DCS with wavelength 6 Å after subtracting scattering from KC_{24}. Solid red lines indicate instrument resolution.

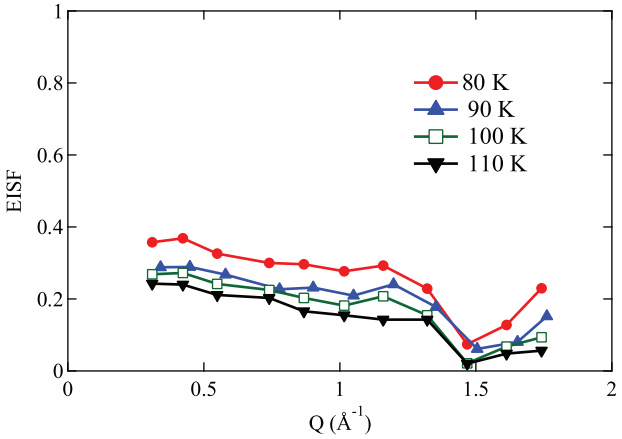

FIG. 5. Experimental EISF values for fits of HC model to $KC_{24}(H_2)_{0.5}$ data.

Experimental QENS spectra were fitted to Eq. (7) simultaneously over all Q-groups, using a single Q-independent adjustable parameter (τ) for the residence time. The jump length l was fixed at the $\sqrt{7} \times \sqrt{7}$ NN distance of 3.7 Å, as we found that making l an adjustable parameter did not improve the quality of fits. The amplitudes (A in Eq. (7)) were fitted independently for each Q-group. We explored fits using both a single EISF (f in Eq. (7)) for all Q-groups, as well as an independently-varying EISF. Allowing the EISF to vary with Q improves the quality of fits as expected, but does not greatly affect the final fitted values for τ. The fitted EISFs are approximately constant as a function of Q, as shown in Fig. 5. At $Q = 1.47$ Å^{-1} and 1.67 Å^{-1}, however, the EISF dips to zero. This may simply be an artifact from the masked (002) KC_{24} diffraction peak located near 1.47 Å^{-1}. All results reported here correspond to fits in which the EISF varies with Q, although the physical meaning of these EISF values remains unclear.

An example of the fits to experimental data at 100 K are shown in Fig. 6. Fits for the remaining 80, 90, and 110 K QENS data are available (see Figs. S1–S3 of the supplementary material[41]). There are small discrepancies between the HC model and the measured QENS data, particularly in the spectrum wings (at low temperatures), and in the spectrum peaks (at higher temperatures). Overall, the HC model outperforms the isotropic jump-diffusion models in terms of accurately fitting $KC_{24}(H_2)_{0.5}$ data across the entire range of Q while using far fewer adjustable parameters. Isotropic models, on the other hand, appear to be better for modeling hydrogen diffusion in zeolites and carbons with larger pore dimensions, where the hydrogen is less sensitive to the host geometry.

The fitted parameters from the HC model are summarized in Table II. Hydrogen residence times on the honeycomb net sites vary from 9 ps at 80 K to approximately 4 ps at 110 K. The H_2 self-diffusion coefficient in $KC_{24}(H_2)_{0.5}$ varied from 3.6 and 8.5 $\times$ 10^{-9} m^2 s^{-1} between 80 K and 110 K, respectively. The temperature dependence of the experimental D follows the Arrhenius equation for a thermally activated process,

$$D = D_0 e^{-E_a/T}, \tag{9}$$

with values of $D_0 = 6.8 \times 10^{-8}$ m^2 s^{-1} and $E_a = 238$ K. For comparison, the activation energy for liquid H_2 near 20 K is approximately 44 K, with a pre-exponential coefficient of 9.1×10^{-9} m^2 s^{-1}.[42]

In the low-Q limit QENS data are less sensitive to individual hops, approaching the limiting form for continuous diffusion in two dimensions. As a comparison to the HC model, therefore, we fitted the smallest Q-group ($Q = 0.31$ Å^{-1}) spectra to the expression in Eq. (8) for continuous diffusion

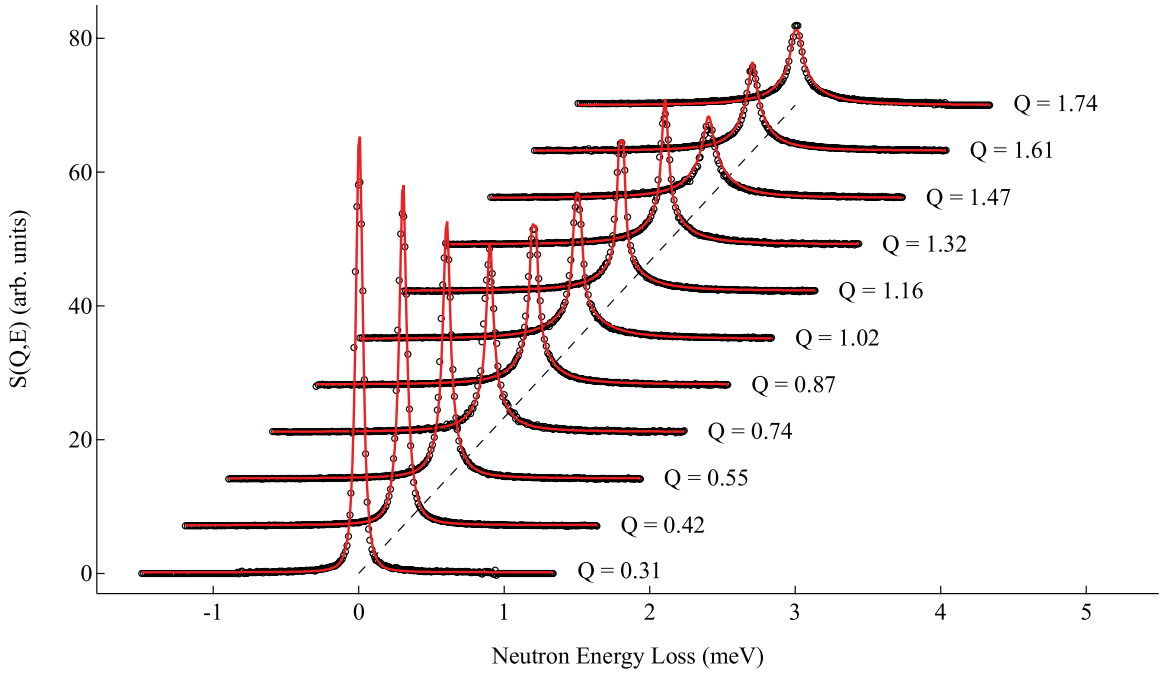

FIG. 6. QENS spectra of $KC_{24}(H_2)_{0.5}$ at 100 K fitted to the honeycomb net jump diffusion model.

TABLE II. Honeycomb net jump diffusion model parameters for $KC_{24}(H_2)_{0.5}$.

T (K)	τ (ps)	l (Å)	D (10^{-9} m^2 s^{-1})
80	9.5	3.7	3.6
90	7.3	3.7	4.7
100	6.0	3.7	5.7
110	4.0	3.7	8.5

in two-dimensions (see Fig. S4 of the supplementary material). The powder average was calculated, followed by numerical convolution with instrument resolution and fitting to the $Q = 0.31$ Å^{-1} data at 80 K–110 K. The self-diffusion coefficients obtained from the 2D model varied from 1.6 $\times 10^{-9}$ m^2 s^{-1} at 80 K to 4.2 $\times 10^{-9}$ m^2 s^{-1} at 110 K, roughly in agreement with the values from the HC model. However, the 2D diffusion model is fitted only to data from a single Q-group where the amount of quasielastic broadening was small. Therefore, significant errors can be expected for the fitted parameters. Interestingly, we found that it was not necessary to include an additional elastic-like term to the 2D continuous diffusion model.

Data in the large-Q limit correspond to a shorter length-scale and consequently are less affected by the two-dimensional geometry of the hydrogen diffusion. We fitted the $KC_{24}(H_2)_{0.5}$ spectra from the seven largest Q-groups (0.87–1.74 Å) to the sum of an elastic peak (delta function) and quasielastic peak (Lorentzian)—a method which is typically applied for isotropic three-dimensional diffusion of molecular hydrogen in solid adsorbents (see Figs. S5–S8 of the supplementary material). Variation of the Lorentzian HWHM versus Q is described by the isotropic jump diffusion model, which has been previously utilized to describe H_2 diffusion in zeolites and carbons.[43–46] This model assumes jumps of variable length in random directions, with a length distribution given by $a(l) = l \exp(-l/l_0)$.[29,47] Parameters obtained from this variable-jump-length isotropic diffusion model were similar to those obtained from the honeycomb net model, although their variation with temperature was smaller. The fitted diffusion coefficients varied between 4.0 $\times 10^{-9}$ m^2 s^{-1} at 80 K and 5.3 $\times 10^{-9}$ m^2 s^{-1} at 110 K. Estimated residence times varied from 5.8 ps at 80 K to 3.5 ps at 110 K.

V. MOLECULAR DYNAMICS SIMULATIONS

Molecular dynamics trajectories for the 1 H_2/K concentration were performed at temperatures of 50 K, 70 K, and 90 K (see Fig. S13 of the supplementary material). The 1 H_2/K concentration is used here rather than the 0.5 H_2/K concentration used in QENS measurements. This gave more hydrogen molecules in the box and improved statistics. The hydrogen molecules rattle around within the triangular potassium cages for extended periods of time before jumping into a neighboring triangular site. There is no diffusion of the potassium atoms at these temperatures, although in the 90 K simulation several of the potassiums do hop out of their initial configurations in the $\sqrt{7} \times \sqrt{7}$ $R19.11°$ superstructure by the end of the simulation. Another interesting feature of the hydrogen dynamics is the formation of regions with increased local H_2 density (clouds), leading to a non-uniform H_2 density throughout the KC_{24} layer planes. Where the hydrogen clouds are best defined, it appears they drift on a scale of hundreds of picoseconds. Hydrogens located on the cloud periphery diffuse more freely compared to those in the cloud interior. These results suggest that large variations in local H_2 concentration may have a large impact on H_2 diffusivity in KC_{24}.

The mean square displacements (MSD) for all 64 hydrogen trajectories were calculated for the 500 ps simulations (see Fig. S14 of the supplementary material). The two dimensional self-diffusion coefficients were calculated from the slope of the MSD using the Einstein relation in the region 50–400 ps. For all temperatures, the MSD has a linear profile between 50 ps and 500 ps. At 50 K, the simulated diffusion coefficient is 2.2 $\times 10^{-9}$ m^2 s^{-1}, increasing to 4.3 $\times 10^{-9}$ m^2 s^{-1} at 70 K and 7.9 $\times 10^{-9}$ m^2 s^{-1} at 90 K. The activation energy is approximately $E_a = 141$ K for the simulated values. Simulated and experimental Ds are compared in Fig. 7. Considering the approximations made in the MD simulations—particularly the absence of an electrostatic interaction term, the 1 H_2/K loading, and the use of an over-simplified $\sqrt{7} \times \sqrt{7}$ $R19.11°$ structure (which does not factor in the higher metal density domain wall regions)—the agreement between experimental and simulated values is excellent.

Simulations were also performed at 90 K at variable H_2 concentrations between 0.25 and 1.75 H_2/K. Powder-averaged incoherent intermediate scattering functions (ISF) were calculated from the MD trajectories at $Q = 1$ Å^{-1} at $T = 90$ K (Fig. S14). The effect of correlation and site-blocking on the ISF lineshape becomes noticeable above a concentration of $x = 1$. At $x = 0.5$, however, the lineshape is very similar to the neighboring 0.75 and 0.25 concentra-

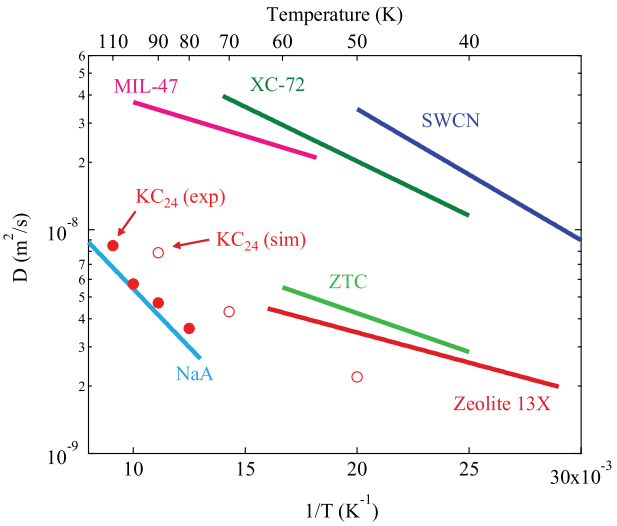

FIG. 7. Comparison of hydrogen diffusivity in a variety of adsorbents. Experimental (solid circle) and simulated (open circle) H_2 self-diffusion coefficients in KC_{24}. Literature values for single-walled carbon nanotubes (SWCN), carbon black (XC-72), zeolite-templated carbon (ZTC), type A zeolite (NaA), type X zeolite (13X), and metal-organic framework (MIL-47) are included for comparison.

tions, and the dilute-limit approximation appears valid. We applied the HC jump diffusion model to experimental QENS data only in the dilute region ($x = 0.5$).

VI. DISCUSSION

Hydrogen diffusivity in KC_{24} is compared in Fig. 7 to values for single-walled carbon nanotubes,[45] zeolite-templated carbon (ZTC),[48] and the conductive carbon black XC-72.[46] Also plotted are self-diffusion coefficients for the NaA zeolite,[43] the 13X zeolite,[44] and the metal-organic framework MIL-47.[49] An obvious feature in Fig. 7 is that values for KC_{24} are an order of magnitude lower than those of the carbons XC-72 and single-walled carbon nanotubes (SWCN). Hydrogen diffuses primarily on external surfaces in XC-72 and SWCNs, which would be expected to present lower diffusion activation barriers compared to KC_{24}. Consistent with this interpretation, the activation energy (E_a) for XC-72 (112 K) and SWCNs (135 K) is appreciably lower than that of KC_{24} (238 K). For MIL-47, hydrogen diffusivity varies strongly with concentration, and the values in Fig. 7 correspond to 3 H_2 per unit cell. Considerably larger diffusivity is observed at lower H_2 loadings.

Hydrogen diffusivity at 77 K in the Mg_2(dobdc) metal-organic framework (i.e., Mg-MOF-74), has been measured at 1.2×10^{-8} m^2 s^{-1} (not shown in Fig. 7), although a large variation is present at low H_2 loading due to strong binding by the open Mg^{2+} coordination sites.[50] Hydrogen diffusion has also been studied by QENS for polyfurfuryl alcohol-derived activated carbon (PFAC) and ultramicroporous activated carbon (UMC),[51] although these measurements are below the temperature range included in Fig. 7. Both materials contain a large fraction of narrow micropores (<10 Å) and may also have other binding sites (e.g., edge terminations). The pre-factors (D_0) for PFAC (2.9×10^{-7} m^2 s^{-1}) and UMC (1.3×10^{-7} m^2 s^{-1}) are significantly larger than that of KC_{24}, indicating larger self-diffusion coefficients. On the other hand, the activation energies for PFAC (219 K) and UMC (179 K) are close that of KC_{24}.

As shown in Fig. 7, hydrogen diffusivity in KC_{24} is closer in value to those of microporous zeolites such as the NaA zeolite. A common feature shared by KC_{24} and the zeolites is that both have strong steric barriers to intracrystalline diffusion. Steric barriers are known to strongly impact the translational diffusion of adsorbed hydrogen molecules as well as other small non-polar molecules.[52] Hydrogen jumps between sorption sites in KC_{24} by passing through narrow windows, in which the energy barrier should be large due to repulsive interactions with the potassium ions and the overlapping graphite corrugation potential. Diffusing H_2 molecules in NaA zeolite must also proceed through narrow windows (4 Å) which connect the larger cavities (11.4 Å). Channels in 13X zeolite are somewhat larger, with an effective diameter of about 8.4–10 Å. Also shown in Fig. 7, the ZTC synthesized from a zeolite NaY starting matrix exhibits H_2 diffusion dynamics very similar to that of zeolite 13X. The ordered microchannels making up the ZTC pore structure have diameters between 5 Å and 20 Å. In comparison, the center-to-center spacing between graphite layers in KC_{24} is approximately 5.4 Å, while the potassiums in the $\sqrt{7} \times \sqrt{7}$ superstructure have a center-to-center distance of 6.5 Å. The effective free diameters of these windows are smaller than the theoretical center-to-center spacings, however. Domain wall regions are also likely to have smaller window diameters due to the greater potassium density.

The potential energy well depths of H_2 sorption sites are measured by equilibrium PCT data. For example, the H_2 adsorption enthalpy for zeolite NaA decreases from −10.7 kJ/mol at 0.5 H_2/cavity to −6.2 kJ/mol at 10 H_2/cavity.[53] Similarly, the adsorption enthalpy of ZTC varies from −7 kJ/mol at 0 wt. % to approximately −3.5 kJ/mol at 1.3 wt. %,[48] with the larger values for NaA perhaps owing to electrostatic binding interactions present for the zeolite. In contrast, the adsorption enthalpy of KC_{24} (see Fig. S12 of the supplementary material) remains relatively constant at approximately −9 kJ/mol from 0.5 H_2/K to 1.8 H_2/K. At low concentration, however, the H_2 binding energies of sorption sites in NaA and KC_{24} are close in value.

Based on the small window apertures between adjacent H_2 sorption sites in the layered KC_{24} structure, one might expect the diffusivity in KC_{24} to be much smaller compared to zeolite NaA. In fact, in a study on hydrogen rotational tunneling in RbC_{24} and CsC_{24}, the authors estimated self-diffusion constants of 9×10^{-10} and 1×10^{-9} m^2 s^{-1} for H_2 in CsC_{24} at 112 K and 125 K, respectively,[12] about a factor of 10 smaller than the values reported in this article. However, the quasielastic peaks were not measured as a function of momentum transfer, a likely source of error, and the sample was CsC_{24} rather than KC_{24}. One possible reason for a larger than expected diffusivity measured in this study is that rotational diffusion was omitted from the analysis. At low temperatures, rotational tunneling is a prominent feature in the $KC_{24}(H_2)_x$ inelastic scattering spectrum.[14] It is known that by coupling to lattice phonons, low-temperature coherent quantum rotation (tunneling) can transform into classical stochastic jump reorientation (diffusion).[54] Increased temperatures would, therefore, produce quasielastic broadening around the elastic line and the tunneling peaks. Temperature dependent broadening of tunneling peaks is in fact observed for CsC_{24}, although it has not yet been studied for KC_{24}. Due to the small radius of the H_2 molecule, however, the rotational contribution to quasielastic broadening is generally small. Few prior studies of hydrogen diffusion utilizing the QENS technique have included rotational diffusion as a part of the analysis.

VII. CONCLUSIONS

Hydrogen self-diffusion in $KC_{24}(H_2)_{0.5}$ was studied with QENS measurements and MD simulations over a temperature range of 80 K–110 K. Diffusivity in KC_{24} is over an order of magnitude smaller than in other carbon adsorbents, but it is similar in value to diffusivities for molecular-sieve zeolites. Self-diffusion coefficients varied from 3.6×10^{-9} m^2 s^{-1} at 80 K to 8.5×10^{-9} m^2 s^{-1} at 110 K. Large activation energy barriers due to (a) the deep potential wells at KC_{24} sorption sites and (b) the narrow windows between adjacent sites, play a significant role in hindering the H_2 self-

diffusion. Good agreement is observed between the experimental and simulated hydrogen diffusivity in KC_{24}. Hydrogen adsorption kinetics in stage-2 AM-GICs at 77 K are found to vary strongly with the adsorbed hydrogen concentration.

ACKNOWLEDGMENTS

The authors thank Ron Cappelletti at NCNR for very helpful discussions, and acknowledge Hillary Smith for help with the QENS measurements. The work benefited from software developed in the DANSE project under National Science Foundation (NSF) Award No. DMR-0520547. This work utilized facilities supported in part by the National Science Foundation under Agreement No. DMR-0944772 and was partially supported by the Office of Energy Efficiency and Renewable Energy through the Hydrogen Sorption Center of Excellence under Contract Nos. DE-FC36-05GO15079 and DE-EE0000262. Certain commercial equipment, instruments, materials, or material suppliers are identified in this article to foster understanding. Such identification does not imply recommendation or endorsement by the National Institute of Standards and Technology, nor does it imply that the materials or equipment identified are necessarily the best available for the purpose.

[1]S. K. Bhatia and A. L. Myers, Langmuir **22**, 1688 (2006).
[2]Y. S. Bae and R. Q. Snurr, Microporous Mesoporous Mater. **132**, 300 (2010).
[3]R. Ströbel, J. Garche, P. T. Moseley, L. Jörissen, and G. Wolf, J. Power Sources **159**, 781 (2006).
[4]Q. Wang and J. Johnson, J. Chem. Phys. **110**, 577 (1999).
[5]W.-Q. Deng, X. Xu, and W. A. Goddard, Phys. Rev. Lett. **92**, 166103 (2004).
[6]S. Patchkovskii, J. Tse, S. Yurchenko, L. Zhechkov, T. Heine, and G. Seifert, Proc. Natl. Acad. Sci. U.S.A. **102**, 10439 (2005).
[7]Z. Jin, W. Lu, K. J. O'Neill, P. A. Parilla, L. J. Simpson, C. Kittrell, and J. M. Tour, Chem. Mater. **23**, 923 (2011).
[8]S. Challet, P. Anzais, R. J.-M. Pellenq, O. Isnard, J.-L. Soubeyroux, and L. Duclaux, J. Phys. Chem. Solids **65**, 541 (2004).
[9]K. Watanabe, T. Kondow, M. Soma, T. Onishi, and K. Tamaru, Proc. R. Soc. London, Ser. A **333**, 51 (1973).
[10]P. Lagrange, D. Guerard, J. F. Mareche, and A. Herold, J. Less-Common Met. **131**, 371 (1987).
[11]T. Terai and Y. Takahashi, Synth. Met. **34**, 329 (1989).
[12]J. P. Beaufils, T. Crowley, T. Rayment, R. K. Thomas, and J. W. White, Mol. Phys. **44**, 1257 (1981).
[13]T. Enoki, S. Miyajima, M. Sano, and H. Inokuchi, J. Mater. Res. **5**, 435 (1990).
[14]A. Lovell, F. Fernandez-Alonso, N. T. Skipper, K. Refson, S. M. Bennington, and S. F. Parker, Phys. Rev. Lett. **101**, 126101 (2008).
[15]J. Purewal, B. Keith, C. Ahn, B. Fultz, C. Brown, and M. Tyagi, Phys. Rev. B **79**, 054305 (2009).
[16]E. L. Pace and A. R. Siebert, J. Phys. Chem. **63**, 1398 (1959).
[17]C. Brown, Y. Liu, T. Yildirim, V. Peterson, and C. Kepert, Nanotechnology **20**, 204025 (2009).
[18]A. Ramirez-Cuesta, P. Mitchell, D. Ross, P. Georgiev, P. Anderson, H. Langmi, and D. Book, J. Mater. Chem. **17**, 2533 (2007).
[19]K. Ichimura, E. Takamura, and M. Sano, Synth. Met. **40**, 355 (1991).
[20]J. R. D. Copley and J. C. Cook, Chem. Phys. **292**, 477 (2003).
[21]R. Azuah, L. Kneller, Y. Qui, P. Tregenna-Piggott, C. Brown, J. Copley, and R. Dimeo, J. Res. Natl. Inst. Stand. Technol. **114**, 341 (2009).
[22]A. Meyer, R. M. Dimeo, P. M. Gehring, and D. A. Neumann, Rev. Sci. Instrum. **74**, 2759 (2003).
[23]G. Chen, Y. Guo, N. Karasawa, and W. A. Goddard, Phys. Rev. B **48**, 13959 (1993).
[24]D. Y. Sun, J. W. Liu, X. G. Gong, and Z.-F. Liu, Phys. Rev. B **75**, 075425 (2007).
[25]A. V. A. Kumar, H. Jobic, and S. Bhatia, J. Phys. Chem. B **110**, 16666 (2006).
[26]F. Salles, D. Kolokolov, H. Jobic, G. Maurin, P. Llewellyn, T. Devic, C. Serre, and G. Ferey, J. Phys. Chem. C **113**, 7802 (2009).
[27]Because the LJ potentials had a 12 Å cutoff and the graphite structure was held fixed, the use of an A–A stacking sequence did not appear to have a large effect on the results.
[28]J. D. Gale and A. L. Rohl, Mol. Simul. **29**, 291 (2003).
[29]C. T. Chudley and R. J. Elliott, Proc. Phys. Soc. London **77**, 353 (1961).
[30]R. Hempelmann, *Quasielastic Neutron Scattering and Solid State Diffusion* (Oxford University Press, Oxford, 2000), Chap. 5.
[31]J. M. Rowe, K. Sköld, and H. E. Flotow, J. Phys. Chem. Solids **32**, 41 (1971).
[32]U. Stuhr, H. Wipf, R. K. Kremer, H. Mattausch, A. Simon, and J. C. Cook, J. Phys.: Condens. Matter **6**, 147 (1994).
[33]R. Cappelletti, Z. Chowdhuri, T. Udovic, R. Dimeo, B. Haubeck, and A. Maeland, Phys. Rev. B **73**, 224109 (2006).
[34]J. Young and J. Koppel, Phys. Rev **135**, 603 (1964).
[35]A. J. Dianoux, F. Volino, and H. Hervet, Mol. Phys. **30**, 1181 (1975).
[36]R. E. Lechner, Solid State Ionics **77**, 280 (1995).
[37]Note that due to the low equilibrium pressures, the distinction between excess adsorption and absolute adsorption can be neglected here.
[38]H. Murdie, I. A. S. Edwards, and H. Marsh, J. Mater. Sci. **20**, 171 (1985).
[39]H. Inokuchi, N. Wakayama, T. Kondow, and Y. Mori, J. Chem. Phys. **46**, 837 (1967).
[40]T. Lu, E. M. Goldfield, and S. K. Gray, J. Phys. Chem. B **110**, 1742 (2006).
[41]See supplementary material at http://dx.doi.org/10.1063/1.4767055 for Figures S1–S14.
[42]D. E. O'Reilly and E. M. Peterson, J. Chem. Phys. **66**, 934 (1977).
[43]R. Kahn and E. V. E. C. De Lara, J. Chem. Phys. **91**, 5097 (1989).
[44]H. Fu, F. Trouw, and P. E. Sokol, J. Low Temp. Phys. **116**, 149 (1999).
[45]D. G. Narehood, J. V. Pearce, P. C. Eklund, P. E. Sokol, R. E. Lechner, J. Pieper, J. R. D. Copley, and J. C. Cook, Phys. Rev. B **67**, 205409 (2003).
[46]O.-E. Haas, J. M. Simon, S. Kjelstrup, A. L. Ramstad, and P. Fouquet, J. Phys. Chem. C **112**, 3121 (2008).
[47]P. A. Egelstaff, *An Introduction to the Liquid State* (Academic, London, 1967), Chap. 10.
[48]Y. Yang, C. M. Brown, C. Zhao, A. L. Chaffee, B. Nick, D. Zhao, P. A. Webley, J. Schalch, J. M. Simmons, and Y. Liu, Carbon **49**, 1305 (2011).
[49]F. Salles, H. Jobic, G. Maurin, M. Koza, P. Llewellyn, T. Devic, C. Serre, and G. Ferey, Phys. Rev. Lett. **100**, 245901 (2008).
[50]K. Sumida, C. M. Brown, Z. R. Herm, S. Chavan, S. Bordiga, and J. R. Long, Chem. Commun. **47**, 1157 (2011).
[51]C. I. Contescu, D. Saha, N. C. Gallego, E. Mamontov, A. I. Kolesnikov, and V. V. Bhat, Carbon **50**, 1071 (2012).
[52]R. M. Barrer, Adv. Chem. **102**, 1 (1971).
[53]F. Stéphanie-Victoire, A.-M. Goulay, and E. Cohen de Lara, Langmuir **14**, 7255 (1998).
[54]M. Prager and A. Heidemann, Chem. Rev. **97**, 2933 (1997).